



One-dimensional ZnO nanostructure as an additive anode material for highly stable lithium-ion battery

Hanaiyah Parasdila¹ · Budi Purnama¹ · Hendri Widiyandari^{1,2}

Received: 10 August 2022 / Accepted: 8 November 2022 / Published online: 16 November 2022
© Qatar University and Springer Nature Switzerland AG 2022

Abstract

Graphite is a commonly used anode material in lithium-ion batteries (LIBs). However, graphite still has certain disadvantages in its application as an anode material, namely poor discharge stability. Accordingly, adding zinc oxide (ZnO) can help overcome these drawbacks because ZnO is an anode material with good chemical stability. In the present study, ZnO was synthesized as an additive material for use as an anode using a hydrothermal method. The optimal conditions for the hydrothermal treatment were determined by varying the synthesis temperature and synthesis holding time. Overall, the X-ray diffraction results showed that all the samples formed a crystalline structure with crystal sizes in the range of 97.87–110.66 nm. Based on field-emission scanning electron microscopy imaging, the morphologies of the ZnO samples showed one-dimensional (1-D) nanostructures with variations in temperature and holding time, which caused the different charge–discharge performances of the assembled LIBs. Furthermore, the LIB configured as the synthesized 1-D graphite/ZnO and commercial $\text{LiNi}_{0.8}\text{Co}_{0.1}\text{Mn}_{0.1}\text{O}_2$ showed outstanding stability compared to the other electrode samples, with specific discharge capacities in the range of 325–352 mAh g⁻¹ and a decreased capacity value about 1.93% after 65 cycles. The present study of graphite/ZnO as anodes in exploring the novel highly stable performance of LIBs demonstrates that it can be considered as electrode materials.

Keywords Zinc oxide · ZnO · Hydrothermal · Anode · Lithium-ion battery

1 Introduction

Lithium-ion batteries (LIBs) have been extensively used in portable devices since 1991 because of their low weight and high energy content. Indeed, almost all laptops and cell phones were equipped with LIBs in 2000 [1]. LIBs are the most widely used and preferred types of batteries in portable devices owing to their ability to be recharged, large energy storage capacity, high energy density, and safety [2].

Currently, there is an increasing demand to improve battery efficiency (i.e., large energy storage capacities and cycling performance stability). The main components of a LIB are electrodes, separators, and electrolytes, in which

the anode plays a critical role in determining battery performance. Moreover, the battery anode operates at a high voltage resulting in a high LIB-specific output capacity [3]. Despite extensive research and development, LIB anodes have problems that limit their applications at a large scale, such as a short lifetime. Therefore, research on promising anode material candidates that can reduce battery shortages is currently underway; for example, an affordable material that can perform and maintain a stable energy storage capacity over a large number of cycles has been investigated [4].

Graphite is a widely used material in commercial anodes. Graphite provides suitable intercalation and deintercalation medium for lithium, thereby generating a high conductivity and reversible specific capacity. However, graphite exhibits poor structural stability, which decreases the specific capacity output. These drawbacks limit the application of graphite as an anode material in high-performance LIBs [5]. Therefore, the incorporation of additive materials in the active material of anodes can minimize such drawbacks.

The requirements for materials that can be used as anode materials for LIBs are a large capacity, fast electron mobility,

✉ Hendri Widiyandari
hendriwidiyandari@staff.uns.ac.id

¹ Department of Physics, Universitas Sebelas Maret, Jl. Ir. Sutami 36A, Surakarta 57126, Indonesia

² Centre of Excellence for Electrical Energy Storage Technology, Universitas Sebelas Maret, Jl. Slamet Riyadi 435, Surakarta 57146, Indonesia

good chemical stability, and long cycle rate [6]. Based on these characteristics, metal oxides meet the criteria for use as additive anode active materials in LIBs. A metal oxide is often used as an anode active material for LIBs for enhanced cycle performance owing to its morphology that can form nanostructures. Metal oxide materials such as Mn_3O_4 [7], SnO_2 [8], Co_3O_4 [9], and TiO_2 [10] have been studied for lithium-ion anodes. Another metal oxide material that also fulfills the material requirements of anode LIBs is zinc oxide (ZnO). ZnO has several advantages over other metal oxides, such as ease of preparation, good chemical stability, low cost [11], and high abundance [12], making it a promising anode material in LIBs. In addition, mixing ZnO with conductive carbon materials, such as commercial graphite, is considered the simplest method to overcome the disadvantages of graphite [13].

In this study, the ZnO is synthesized using a simple hydrothermal process, which has been demonstrated as the most promising process for fabricating well-crystallized structures [14]. It is an energy-efficient process for synthesizing ZnO with excellent crystallinity and nanostructure [15]. Widiyandari et al. (2021) [16] asserted that a high-temperature hydrothermal process would also result in a larger crystal size. Additionally, the hydrothermal method is environmentally friendly and economically feasible [17]. Furthermore, the produced ZnO nanostructure material was used as an additive material for the active material of a LIB anode. This improved the stability of the cycle performance of LIBs.

2 Methodology

2.1 Synthesis

ZnO material was synthesized from 1 M zinc nitrate hexahydrate ($\text{Zn}(\text{NO}_3)_2 \cdot 4\text{H}_2\text{O}$, 99% Sigma Aldrich) and 0.5 M hexamethylenetetramine (HMTA, $\text{C}_6\text{H}_{12}\text{N}_4$, Supelco) with 40 mL distilled water as a solvent via the hydrothermal method. The precursor solution was stirred for 1 h using a magnetic stirrer and then placed in an autoclave for the hydrothermal process. During the hydrothermal process, the synthesis temperature was varied 100–160 °C at constant holding time of 6 h. The resulting ZnO samples were named ZnO-100, ZnO-120, ZnO-140, and ZnO-160 to indicate the variation in the synthesis temperature. Then, the holding time was varied (3–12 h), while the temperature was maintained at 140 °C using a furnace. The samples were named ZnO-3 h, ZnO-6 h, ZnO-9 h, and ZnO-12 h to indicate the variation in the synthesis holding time. After the hydrothermal process was complete, the resulting solution was filtered and washed using distilled water until neutral pH was reached, dried in an oven at 80 °C, and annealed at 450 °C

for 2 h for the crystallization process. The resulting ZnO powder was then characterized.

2.2 Material characterization

The ZnO powder was characterized using X-ray diffraction (XRD, Rigaku Smartlab, Japan) to determine the crystal structure and crystal size using $\text{Cu K}\alpha$ radiation ($\lambda = 1.5406 \text{ \AA}$) in the range of 10–90°. The morphology of the ZnO samples was characterized using field-emission-scanning electron microscopy (FE-SEM, JEOL JIB-4610F, Japan), and the elemental composition of ZnO and the presence of impurities in ZnO were characterized using energy dispersive X-ray (EDX, JEOL JIB-4610F, Japan).

2.3 Battery cell assembly

To produce the LIB anodes, the characterized samples (ZnO) were mixed with graphite (Gelion LIB. Co. Ltd., China) in the ratio 1:9. Acetylene black (AB, Gelion LIB. Co. Ltd., China) and binders styrene butadiene rubber (SBR, Gelion LIB. Co. Ltd., China) and carboxymethyl cellulose (CMC, Gelion LIB. Co. Ltd., China) in the ratio of 80:10:7:3 for 4 g base using distilled water as the solvent. The mixture was stirred for 2 h to obtain a paste. The resulting paste was coated with a thin layer on top of the Cu foil using the doctor blade method, which was then placed in an oven until dry. This anode manufacturing protocol followed that of a previous study by Yudha et al. [18].

The resulting anode film was used to assemble a full-cell battery with 18,650 cylindrical lithium-ion components in a separator-anode-separator-cathode arrangement. The batteries were then assembled in a glove box filled with an electrolyte solution. LiPF_6 was used as the electrolyte. Electrolytes containing LiPF_6 usually exhibit good conductivity and electrochemical stability and do not promote aluminum corrosion.

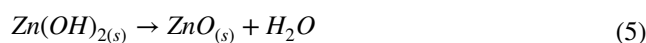
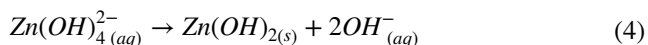
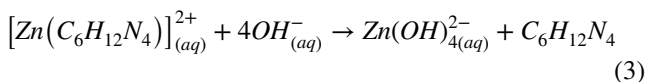
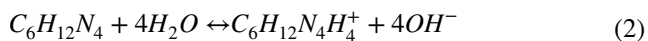
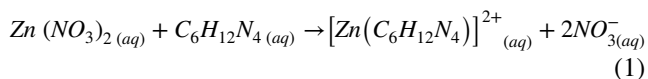
2.4 Electrochemical measurements

The full cell battery with 18,650 cylindrical cell type LIBs was tested using eight channel battery analyzers (BTS-5V6A, Neware, China) to obtain the battery charge–discharge capacity. These tests were the capacity test/formation test at 0.05 C for three cycles, rate capability for slow (0.1 C and 0.2 C), standard (1 C), and fast (2 C) charging for three cycles each, and cycle performance at standard charging of 1 C for 65 cycles. Subsequently, the LIBs were tested using electrochemical impedance spectroscopy (EIS, EZstat Pro Nuvant) to determine the resistance value of LIBs in the frequency range of 0.01 Hz–10 kHz and an amplitude of 5 mV. The impedance data obtained would be fit using Zsimp 3.2 software to obtain the battery resistance value.

3 Results and discussion

3.1 Crystallinity and morphology of ZnO

The ZnO samples produced in this study were synthesized using a hydrothermal method involving zinc nitrate hexahydrate and HMTA in distilled water. The chemical reactions that occurred in this hydrothermal process are shown in Eqs. (1)–(5) [19]:



HMTA is a stronger Lewis base than water and tetradentate ligand. It can displace water and chelate Zn^{2+} ions through four N atoms (Eq. (1)). HMTA also acts as a source of OH^- ions (Eq. (2)), which displaces the bonding with the Zn-HMTA complex and forms $\text{Zn}(\text{OH})_4^{2-}$ (Eq. (3)). Heat causes $\text{Zn}(\text{OH})_4^{2-}$ to precipitate as $\text{Zn}(\text{OH})_2$ (Eq. (4) and (5)) and form ZnO upon drying.

Figure 1(a–b) shows the XRD patterns of the ZnO samples. The observed peaks are sharp and narrow, indicating that the samples formed crystalline structures. The clearly visible peaks match with the International Centre for Diffraction Data (ICDD) reference No. 89–1397, indicating that ZnO has a hexagonal crystal structure with lattice parameters $a = b \neq c$. The crystallite size of the ZnO samples is calculated using the Scherrer equation at the highest peak (101), as shown in Table 1.

From phase identification using XRD, it can be seen that the crystalline sizes of the ZnO-100 and ZnO-120 samples increase with increasing heating temperature, as was

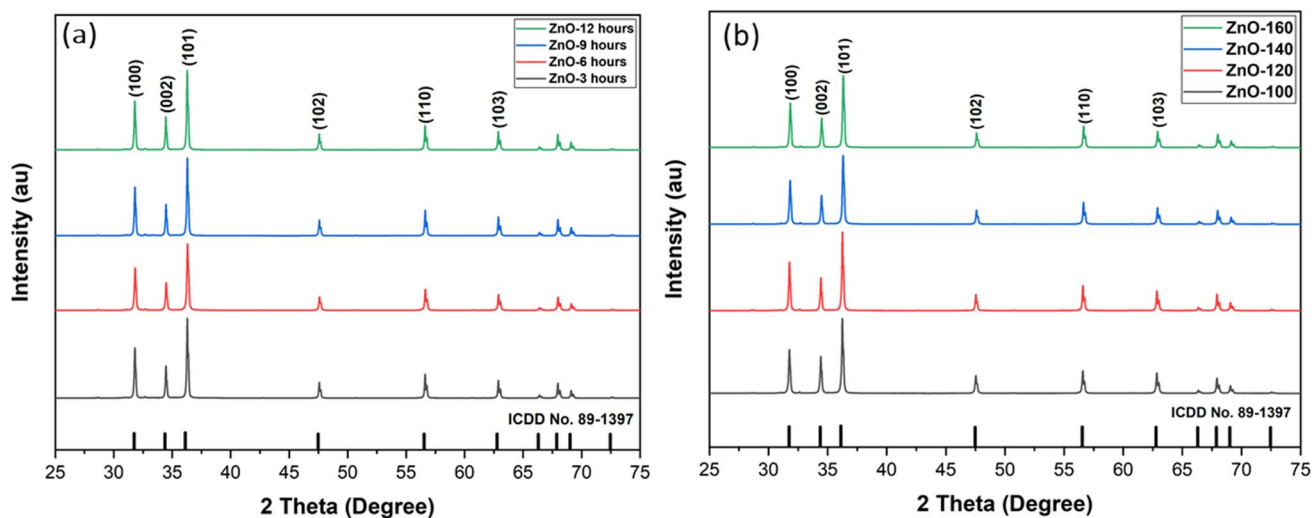


Fig. 1 Diffraction patterns of ZnO with variations in (a) holding time and (b) temperature

Table 1 Crystalline sizes of ZnO samples

Variation	Sample	2 θ (°)	FWHM (°)	Crystalline size (nm)
Temperature of synthesis	ZnO-100	36.26	0.1907	103.32
	ZnO-120	36.26	0.1835	107.38
	ZnO-140	36.29	0.2014	97.87
	ZnO-160	36.31	0.1889	104.37
Holding time of synthesis	ZnO-3 h	36.3	0.1904	103.54
	ZnO-6 h	36.27	0.2014	97.87
	ZnO-9 h	36.31	0.1787	110.33
	ZnO-12 h	36.41	0.1784	110.66

previously reported [20]. However, in the ZnO-140 and ZnO-160 samples, the highest peak widens and has a low intensity (Fig. 2(b)), resulting in a smaller crystal size. The low crystallinity and peak widening indicate the presence of crystal defects in the sample [21].

As presented in Table 1, based on the synthesis holding time, the variation in the crystalline sizes of ZnO-3 h (103.54 nm), ZnO-9 h (110.33 nm), and ZnO-12 h (110.66 nm). However, according to Fig. 2(a), the ZnO-6 h sample also showed peak widening and a low intensity,

which indicates a crystal defect similar to samples ZnO-140 and ZnO-160.

FE-SEM imaging shows that the ZnO particles tend to agglomerate at all synthesis temperatures. In addition, the samples (Figs. 3 and 4) have different morphologies for every variation of synthesis temperature and synthesis holding time. The ZnO-100 sample (Fig. 4(a)) forms a nano-flower structure, while the ZnO-120 (Fig. 4(b)) and ZnO-160 (Fig. 4(d)) samples form deformed spherical particles agglomerated and assembled into nanorods, which is in

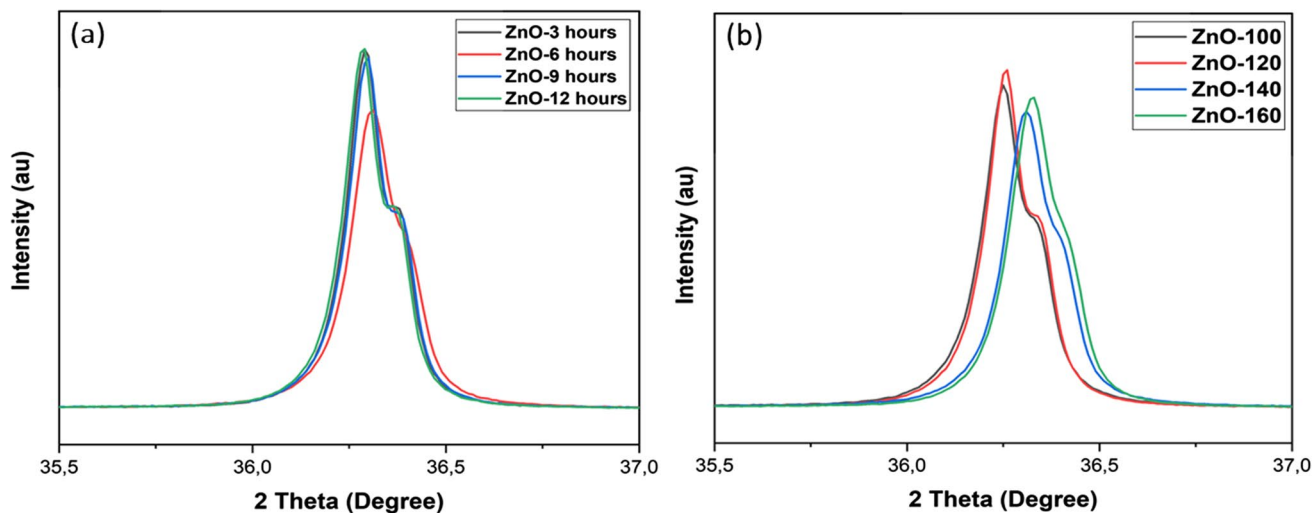


Fig. 2 Highest peak (101) of ZnO (a) holding time and (b) temperature

Fig. 3 Morphology images of (a) ZnO-3 h, (b) ZnO-6 h, (c) ZnO-9 h, and (d) ZnO-12 h

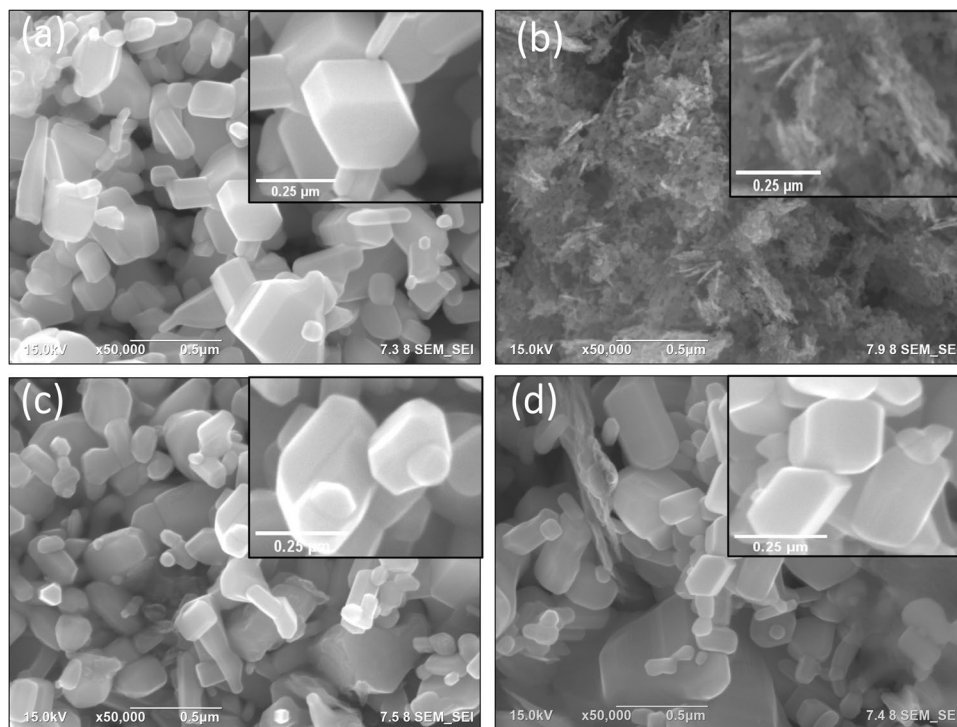
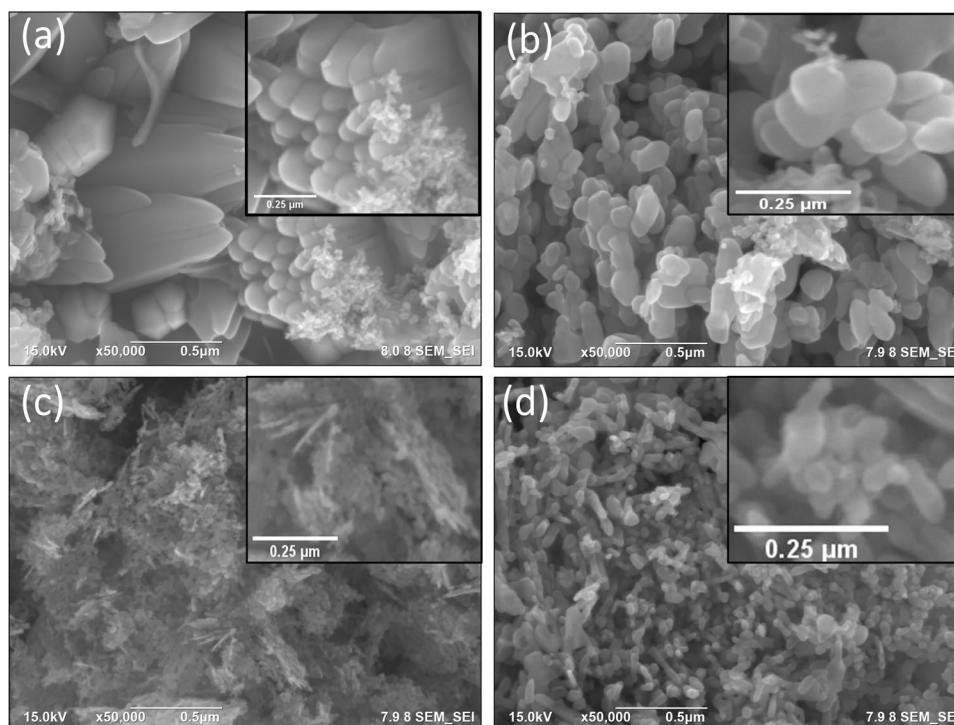


Fig. 4 Morphology images of (a) ZnO-100, (b) ZnO-120, (c) ZnO-140, and (d) ZnO-160



accordance with previously reported results [22]. Agglomeration occurs because the ZnO colloids tend to agglomerate easily at low temperatures, yielding a non-uniform particle size at low temperatures [23]. These differences in structures may be attributed to the different amounts of heat energy supplied during synthesis, causing the reaction rate to differ and the ZnO growth has its own phase in forming the ZnO structure.

In contrast to the variation in synthesis temperature, which affects the morphology, the variation in holding time yields a nearly uniform nanorod morphology for the ZnO samples (Fig. 3(a–d)), except for the sample with a holding time of 6 h. The morphology of this sample shows a great similarity to that produced at a synthesis temperature of 140 °C. The variation in the holding time causes the particle distribution to become narrower, resulting in a more homogeneous structure.

The ZnO-140 (Fig. 4(c)) and ZnO-6 h (Fig. 3(b)) samples form nanoflakes, similar to those previously reported [24], which were synthesized using a hydrothermal process at 150 °C. Wahyuningsih et al. [24] stated that temperature affects aggregation under neutral conditions yielding 3-D ZnO nanoflowers at a given treatment time. In LIBs, ZnO nanostructures are preferred because they increase the conductivity of the ZnO electrode and maintain the electrode structure to produce optimum results [25].

Table 2 shows the chemical composition of synthesized ZnO determined using EDX. All the ZnO samples are confirmed to contain Zn and O without any impurities from

Table 2 ZnO sample elemental analysis

Variation	Sample	Mass (%)	
		Zn	O
Temperature of synthesis	ZnO-100	73.68	26.31
	ZnO-120	79.48	20.51
	ZnO-140	76.70	23.29
	ZnO-160	78.98	21.01
Holding time of synthesis	ZnO-3 h	82.75	17.24
	ZnO-6 h	76.70	23.29
	ZnO-9 h	80.68	19.31
	ZnO-12 h	80.09	19.90

other elements. The percentage mass of Zn and O differs in each sample owing to the varying synthesis temperature and holding time. The ZnO-100 sample contains the lowest mass percentage of Zn, while the ZnO-3 h sample contains the highest. The opposite trend is observed for the mass percentage of O.

3.2 Lithium-ion battery electrochemical property

Cylinder 18,650-type LIB full cells with graphite/ZnO as anodes and $\text{LiNi}_{0.8}\text{Co}_{0.1}\text{Mn}_{0.1}\text{O}_2$ as the cathode were used in the battery performance test. The results of the first charge–discharge test carried out on the batteries with the samples produced under varying temperatures and holding times are shown in Figs. 5–6a–d. The results

Fig. 5 Formation phase of charge–discharge of graphite/ZnO anodes of lithium-ion battery (a) graphite/ZnO-3 h, (b) graphite/ZnO-6 h, (c) graphite/ZnO-9 h, and (d) graphite/ZnO-12 h

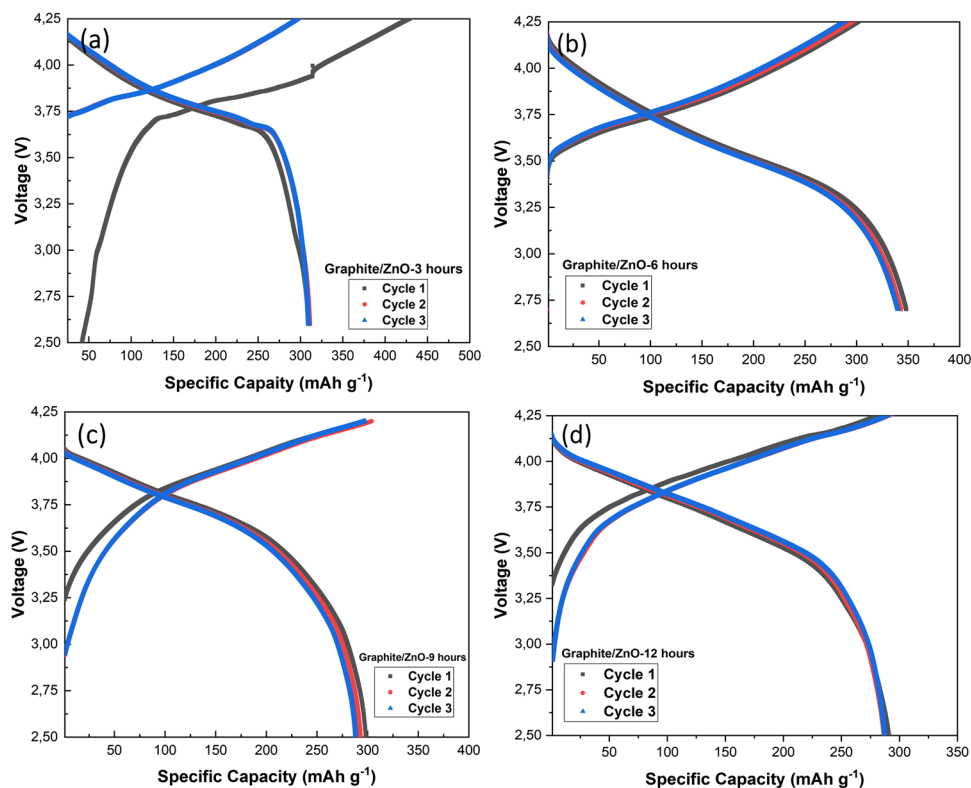
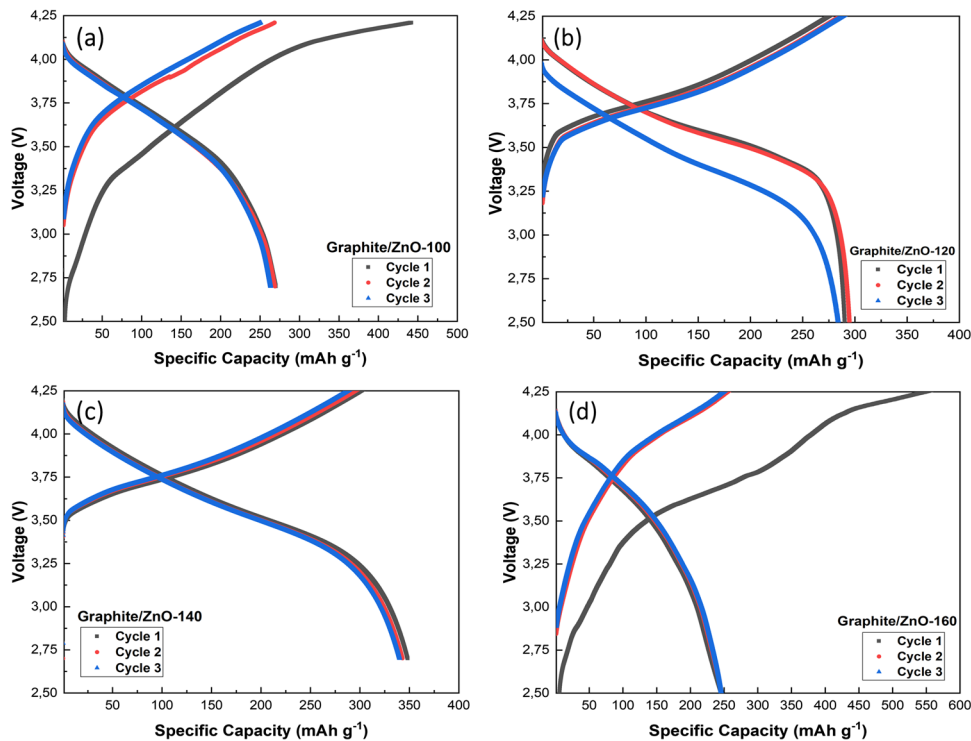


Fig. 6 Formation phase of charge–discharge of graphite/ZnO anodes of lithium-ion battery (a) graphite/ZnO-100, (b) graphite/ZnO-120, (c) graphite/ZnO-140, and (d) graphite/ZnO-160



of charging and discharging of a LIB are illustrated with increasing and decreasing voltages, respectively. In the initial charge–discharge test, LIBs with different graphite/ZnO-based anode variations were tested with the same

current, which was 0.05 C. During the charging process, Li^+ intercalates into the anode material, and during the discharging process, Li^+ undergoes de-intercalation from

Fig. 7 1st cycle of charge–discharge curves of graphite/ZnO anodes of lithium-ion battery (a) holding time and (b) temperature

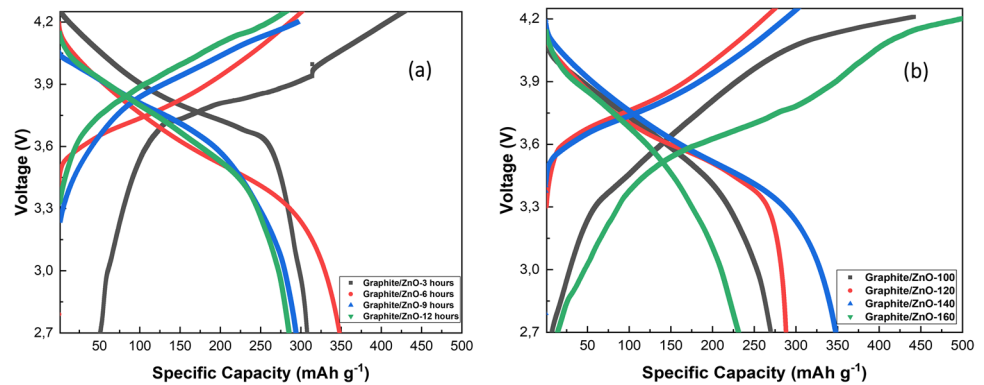


Table 3 Coulombic efficiency of graphite/ZnO anodes of lithium-ion battery

Variation	Cycle number	Cycle 1 (%)	Cycle 2 (%)	Cycle 3 (%)
Temperature of synthesis	Graphite/ZnO-100	49	92	95
	Graphite/ZnO-120	100	98	93
	Graphite/ZnO-140	97	98	98
	Graphite/ZnO-160	40	89	92
Holding time of synthesis	Graphite/ZnO-3 h	66	96	96
	Graphite/ZnO-6 h	97	98	98
	Graphite/ZnO-9 h	100	96	96
	Graphite/ZnO-12 h	96	92	93

the anode material into the cathode. The first cycle of this test is considered the formation phase or capacity [26].

Based on Fig. 7(a–b), in the first cycle, the LIBs appear to have different charge–discharge capacities. This may be because of the morphological characteristics of the prepared samples. The smaller particles and larger surface area promote side reactions between the material and electrolyte during the first charge, called the solid electrolyte interface (SEI) process [27]. An SEI is formed when the electrode (metal) is in contact with the electrolyte (solution), and this causes a reduction in the number of lithium ions accommodated by the anode. As a result, the number of SEI layers increases during the first charge and discharge cycle, causing a further reduction in the total capacity and starting stability in the second and subsequent cycles [28].

In this first formation process, graphite/ZnO-140 and graphite/ZnO-6 h have specific discharge capacities that are relatively stable and the highest among the samples at 348.23 mAh g⁻¹. This excellent performance is reinforced by the coulombic efficiency (CE) demonstrated (Table 3). Upon entering the second and third cycles, the charge–discharge tests of graphite/ZnO-140 and graphite/ZnO-6 h exhibit the most stable CE value among the samples. CE itself illustrates the comparison between the number of Li⁺ ions or electrons returning to the cathode and the number of Li⁺ or electrons leaving the cathode in one full cycle [29]. This indicates that the electrode samples composed of graphite/

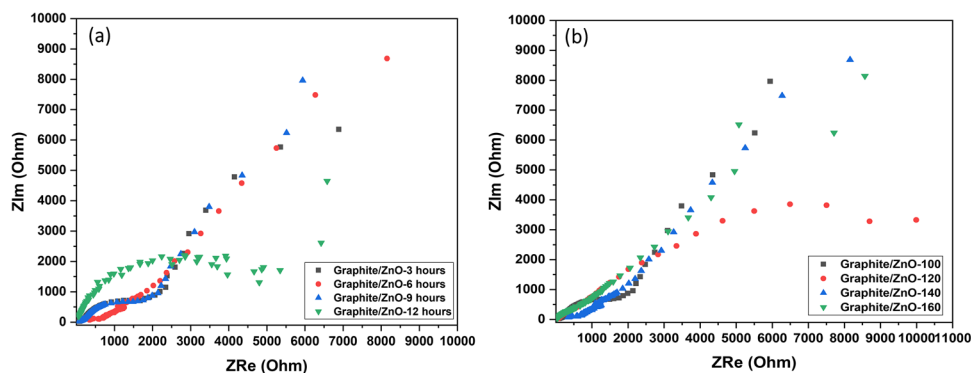
Table 4 Charge transfer resistance (R_{ct}) of graphite/ZnO anodes of lithium-ion battery

Variation	Sample	R_{ct} (Ohm)
Temperature of synthesis	Graphite/ZnO-100	634.6
	Graphite/ZnO-120	127.9
	Graphite/ZnO-140	96.52
	Graphite/ZnO-160	204.6
Holding time of synthesis	Graphite/ZnO-3 h	75.04
	Graphite/ZnO-6 h	96.52
	Graphite/ZnO-9 h	636.2
	Graphite/ZnO-12 h	602.9

ZnO-140 and graphite/ZnO-6 h have the highest Li⁺ ion storage capacity compared to the other samples.

The transfer coefficients obtained from the EIS test, which analyzes the R_{ct} (charge transfer resistance) value of LIBs, are shown in Table 4, and the R_{ct} data were obtained from the Nyquist plot, as illustrated in Fig. 8. Table 4 shows that the R_{ct} values of the graphite/ZnO-140 and graphite/ZnO-6 h samples are smaller, approximately 96.52 Ω . This implies that graphite/ZnO-140 and graphite/ZnO-6 h have better electron transfer capabilities than the other samples. This is also influenced by the small crystal size and particle diameter, as shown by FE-SEM imaging, which enlarges the particle surface area for lithium intercalation.

Fig. 8 Nyquist plot of graphite/ZnO anodes of lithium-ion battery (a) holding time and (b) temperature



After the first charge–discharge process and the formation phase for three cycles, the LIB was charged and discharged at various levels. Figure 9(a–b) shows the rate capability of all the anodes of the graphite/ZnO samples. Further, all the graphite/ZnO-based anodes show the same pattern: a decrease in the discharging capacity is obtained as the inrush current increases. However, the highest capacity value is exhibited by the graphite/ZnO-6 h and graphite/ZnO-140 electrodes, which is $342.16 \text{ mAh g}^{-1}$ in the first cycle of 0.1 C current and ends at $289.27 \text{ mAh g}^{-1}$ in the third cycle of the 2 C current, with a decreasing value capacity of 15.45%. This phenomenon often occurs because of the wide range of morphologies of the samples. Figures 3 and 4 confirm that the graphite/ZnO-140 and graphite/ZnO-6 h samples have fine morphologies and the smallest crystal sizes among the samples. According to Liu and Cao [30], after SEI formation, the diffusion of Li^+ ions from the surface to the interior depends on the crystal structure, and crystallinity is a factor that needs to be considered and manipulated to increase the Li^+ ion insertion capacity.

As shown in Fig. 9(a–b), all the samples showed a slight decrease in capacity, even after being discharged at high current rates. At high currents, the battery performance depends on the Li^+ ion mass transfer and kinetics. Although a large surface area encourages side reactions, it can be beneficial during the high-level discharging process [30]. This result shows that the battery with the graphite/ZnO-based anode sample is quite resistant to low and high discharge rates, with a measurable decrease capacity.

In the charge and discharge formation tests and rate-ability tests, which were carried out on the graphite/ZnO electrodes, variations in temperature and holding time were observed. The graphite/ZnO electrode sample obtained at 140 °C and 6 h demonstrates the highest and most stable discharge capacity compared to the other electrode samples. This sample was then used to test the cycle performance of the LIB with a standard charge–discharge current of 1 C for 65 cycles, and the results are shown in Fig. 10.

Figure 10 shows the cycle performance of a LIB using a graphite/ZnO anode compared to that of a commercial

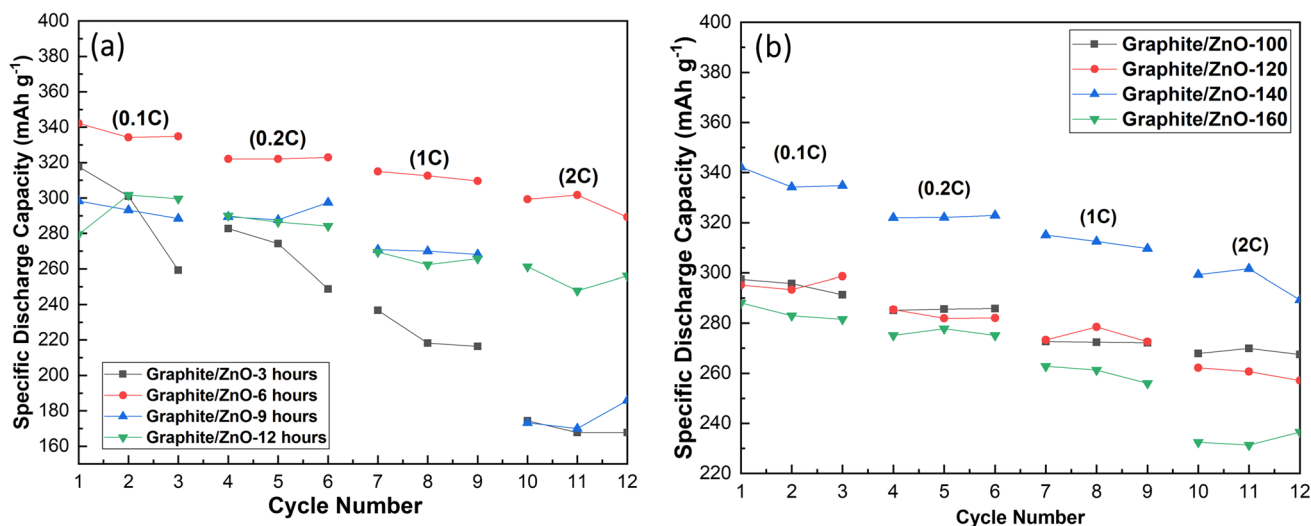


Fig. 9 Rate capability results of graphite/ZnO anodes of lithium-ion battery (a) holding time and (b) temperature

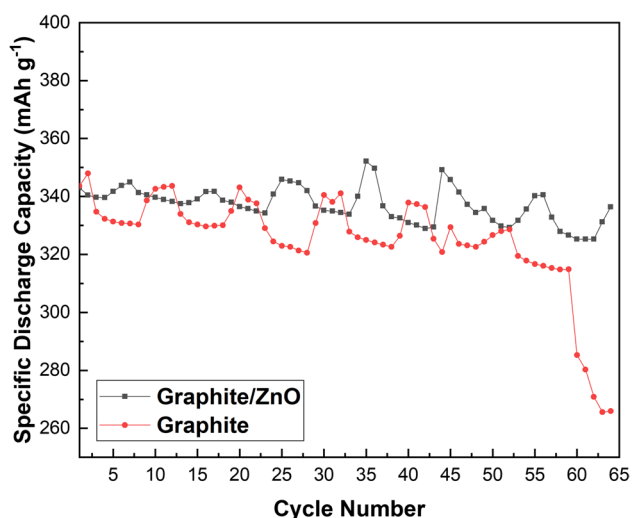


Fig. 10 Cycle performance of lithium-ion battery with graphite/ZnO anodes compared to commercial graphite anode

graphite anode. Graphite/ZnO, as the main active material of the anode of a LIB, yields enhanced stability in discharge capacity performance compared to the commercial graphite anode. In addition to having better stability, the graphite/ZnO electrode sample also has a higher specific discharge capacity in the range of 325–352 mAh g⁻¹ compared to that of commercial graphite, which is in the range of 265.6–343.62 mAh g⁻¹.

Based on the specific discharge capacity obtained over 65 cycles, the graphite/ZnO electrode samples experience a capacity loss of approximately 1.93%, which is lower than the value obtained for commercial graphite after 65 cycles (22.62%). In other words, the graphite/ZnO electrode samples have better stability than commercial graphite electrodes. The smaller the capacity of the battery, the better its stability.

The results of this LIB test are influenced by the graphite/ZnO synthesis treatment, which affects crystal growth and sample morphology; thus, the lithium-ion intercalation process during battery testing also produces different results. Based on the of the LIBs with the graphite/ZnO anode, the synthesis of ZnO, which influences crystal growth and morphology, plays a crucial role in determining the Li⁺ intercalation process. The different crystallinities, as shown by the XRD patterns, may have prompted the difference in performance, especially in terms of capacity [26]. The graphite/ZnO-140 electrode with a holding time of 6 h has the smallest crystal size. Shen et al. [31] reported that the discharge capacity increases as the crystal size decreases.

In addition, the graphite/ZnO-140 sample with a holding time of 6 h has a finer morphology than the other synthesized ZnO samples, based on FE-SEM images. The relatively uniform morphology is beneficial for improving

electrode performance, resulting in shortened ion diffusion and a larger contact surface area with the electrolyte for Li⁺ ion transfer [32]. Thus, the graphite/ZnO-140 electrode with a holding time of 6 h could be a potential candidate in LIB active materials for stabilizing the LIB storage capacity.

4 Conclusion

All the ZnO samples incorporated into the active material of the LIBs were synthesized using the hydrothermal method. Based on the XRD results, ZnO samples were successfully synthesized and formed crystals. FE-SEM observations showed different morphologies based on the hydrothermal treatment conditions: ZnO-100 (nanoflower), ZnO-120, ZnO-160 (spherical to nanorod), ZnO-140 (1-D structure formation), and ZnO with varying holding time (nanorods). The LIB performance test showed that the charge–discharge stability was relatively good and suitable for use, with a specific capacity range measured at 325–352 mAh g⁻¹ and a discharge capacity loss of 1.93% over 65 cycles. In conclusion, ZnO has the potential to be an additive active material for LIB anodes. However, further large-scale research needs to be conducted, particularly on other synthesis methods and the battery assembly processes, to obtain an improved LIB performance.

Acknowledgements The authors are thankful to the Centre of Excellence for Electrical Energy Storage Technology and Sebelas Maret University for providing a battery testing facility.

Author contribution All authors contributed to the study conception and design. Material preparation, data collection and analysis were performed by [Hendri Widiyandari], and [Hanaiyah parasdila]. The first draft of the manuscript was written by [Hanaiyah parasdila] and all authors commented on previous versions of the manuscript. All authors read and approved the final manuscript.

Funding This work was partially supported by the Ministry of Research and Technology/ National Innovation and Research Agency Republic Indonesia [Grant number 221.1/UN27.22/HK.07.00/2021].

Declarations

Conflict of interest The authors declare no competing interests.

References

1. S. Leuthner. Lithium-ion battery overview. In *Lithium-ion batteries: Basics and Applications* (Springer. Berlin, Heidelberg, 2018) 13–19
2. H. Widiyandari, A.N. Sukmawati, H. Sutanto, C. Yudha, A. Purwanto, J. Phys: Conference Series. **1153**, 012074 (2019)
3. X. Chen, Y. Huang, J. Chen, X. Zhang, C. Li, H. Huang, *Ceramics Int.* **41**, 8533 (2015)
4. R. Li, W. Xiao, C. Miao, R. Fang, R. Wang, Z.M. Zhang, *Ceramics Int.* **45**, 13530 (2019)

5. X. Rao, Y. Lou, J. Chen, H. Lu, B. Cheng, W. Wang, H. Fang, H. Li, S. Zhong, *Front. Energy Res.* **8**, 3 (2020)
6. Y.D. Pambudi, S. Setiabudy, R. Yuwono, A.H. Kartini, J.K. Lee, & C. Hudaya. *Ionics.* **25** (2) (2019)
7. N. Jarulertwathana, X. Jin, S.J. Hwang, *Emergent Mater.* **2**, 487 (2019)
8. B. Huang, X. Li, Y. Pei, S. Li, X. Cao, R.C. Massé, G. Cao, *Small* **12**, 1945 (2016)
9. C. Hou, B. Wang, V. Murugadoss, S. Vupputuri, Y. Chao, Z. Guo, C. Wang, W. Du, *Eng.* **11**, 19 (2020)
10. P. Díaz-Carrasco, A. Duarte-Cárdenas, A. Kuhn, F. García-Alvarado, *J. Power Sources.* **515**, 230632 (2021)
11. C. Kim, J.W. Kim, H. Kim, D.H. Kim, C. Choi, Y.S. Jung, J. Park. *Chem. Mater.* **28**, 8498 (2016)
12. F. Sun, J. Gao, H. Wu, X. Liu, L. Wang, X. Pi, Y. Lu, *Carbon* **113**, 46 (2017)
13. R. Guo, Z. Huang, J. Wu, W. Zhong, Y. Lin, Y. Cao, *Ceram. Int.* **46**, 19966–19972 (2020)
14. S. Agarwal, P. Rai, E.N. Gatell, E. Llobet, F. Güell, M. Kumar, K. Awasthi, *Sens. Actuators B Chem.* **292**, 24 (2019)
15. H. Wang, T. Liang, X. Yu, W. Zhao, R. Xu, D. Wang, Y. Liu, *RSC Adv.* **6**, 96882 (2016)
16. H. Widiyandari, O.A. Putra, A. Purwanto, A. Subagio, *Mater. Sci. Eng.* **1096**, 012142 (2021)
17. H. Zhao, F. Li, X. Liu, W. Xiong, B. Chen, H. Shao, D. Que, Z. Zang, Y. Wu, *Electrochem. Acta* **166**, 124 (2015)
18. C.S. Yudha, A.P. Hutama, M. Rahmawati, H. Widiyandari, H. Nursukatmo, H. Nilasary, H.S. Oktaviano, A. Purwanto, *Energies* **14**(18), 5980 (2021)
19. Z. Khusaimi, S. Amizam, M.H. Mamat, M.Z. Sahdan, M.K. Ahmad, N. Abdullah, M. Rusop, *Synth. Reactivity Inorg. Metal-Organic, Nano-Metal Chem.* **40**, 190 (2010)
20. Z.N. Kayani, F. Saleemi, I. Batoool, *App. Phys. A* **119**, 2015 (2015)
21. L. Muñoz-Fernandez, A. Sierra-Fernández, O. Milošević, M.E. Rabanal, *Adv. Powder Tech.* **27**, 983 (2016)
22. W. Widiyastuti, S. Machmudah, T. Nurtono, S. Winardi, R. Balgis, T. Ogi, K. Okuyama, *Chem. Eng. Transactions.* **56**, 955 (2017)
23. M. Shandilya, R. Rai, J. Singh. *Adv. App. Ceramics.* **115**, 354 (2016)
24. S. Wahyuningsih, A.H. Ramelan, E. Pramono, H.P. Nuryana, M.M.A. Mujahidin, H. Munawaroh, R. Hidayat, G. Fadillah, *Chem. Phys. Lett.* **790**, 139351 (2022)
25. K. Ruan, Y. Guo, Y. Tang, Y. Zhang, J. Zhang, M. He, J. Kong, J. Gu. *Compos. Commun.* **10**, 68 (2018)
26. C.S. Yudha, S.U. Muzayanha, H. Widiyandari, F. Iskandar, W. Sutopo, A. Purwanto, *Energies* **12**, 1886 (2019)
27. U.S. Meda, L. Lal, M. Sushantha, & P. Garg. *J. Energy Storage.* 103564 (2021)
28. J. Xiao, Q. Li, Y. Bi, M. Cai, B. Dunn, T. Glossmann, J. Liu, T. Osaka, R. Sugiura, B. Wu, J. Yang, J.G. Zhang, M.S. Whittingham, *Nat. Energy* **5**, 561 (2017)
29. D. Liu, G. Cao, *Energy & Environmental Sci.* **3**, 1218 (2010)
30. I. Hwang, C.W. Lee, J.C. Kim, S. Yoon, *Mater. Research. Bulletin* **47**, 73 (2012)
31. Y. Shen, J.R. Eltzholtz, B.B. Iversen, *Chem. of Mater.* **25**, 5023 (2013)
32. L. Wang, Y. Zhang, M.E. Scofield, S. Yue, C. McBean, A.C. Marschilok, K.J. Takeuchi, E.S. Takeuchi, S.S. Wong, *Chem. Sus. Chem.* **8**, 3304 (2015)

Springer Nature or its licensor (e.g. a society or other partner) holds exclusive rights to this article under a publishing agreement with the author(s) or other rightsholder(s); author self-archiving of the accepted manuscript version of this article is solely governed by the terms of such publishing agreement and applicable law.